



2004

## Grain Size Distributions and Photoelectric Heating in Ionized Media

P. A. M. vanHoof  
*Durham University, UK*

J. C. Weingartner  
*University of Toronto, Canada*

P. G. Martin  
*University of Toronto, Canada*

K. Volk  
*University of Calgary, Canada*

Gary J. Ferland  
*University of Kentucky, gary@uky.edu*

Follow this and additional works at: [https://uknowledge.uky.edu/physastron\\_facpub](https://uknowledge.uky.edu/physastron_facpub)



Part of the [Astrophysics and Astronomy Commons](#), and the [Physics Commons](#)

[Right click to open a feedback form in a new tab to let us know how this document benefits you.](#)

---

### Repository Citation

vanHoof, P. A. M.; Weingartner, J. C.; Martin, P. G.; Volk, K.; and Ferland, Gary J., "Grain Size Distributions and Photoelectric Heating in Ionized Media" (2004). *Physics and Astronomy Faculty Publications*. 45.  
[https://uknowledge.uky.edu/physastron\\_facpub/45](https://uknowledge.uky.edu/physastron_facpub/45)

This Article is brought to you for free and open access by the Physics and Astronomy at UKnowledge. It has been accepted for inclusion in Physics and Astronomy Faculty Publications by an authorized administrator of UKnowledge. For more information, please contact [UKnowledge@lsv.uky.edu](mailto:UKnowledge@lsv.uky.edu).

---

## Grain Size Distributions and Photoelectric Heating in Ionized Media

Digital Object Identifier (DOI)

<http://dx.doi.org/10.1111/j.1365-2966.2004.07734.x>

### Notes/Citation Information

Published in *Monthly Notices of the Royal Astronomical Society*, v. 350, issue 4, p. 1330-1341.

This article has been accepted for publication in *Monthly Notices of the Royal Astronomical Society* ©: 2004 The Authors Published by Oxford University Press on behalf of the Royal Astronomical Society. All rights reserved.

The copyright holder has granted the permission for posting the article here.

# Grain size distributions and photoelectric heating in ionized media

P. A. M. van Hoof,<sup>1,2★†</sup> J. C. Weingartner,<sup>1‡</sup> P. G. Martin,<sup>1</sup> K. Volk<sup>3§</sup> and G. J. Ferland<sup>2</sup>

<sup>1</sup>Canadian Institute for Theoretical Astrophysics, University of Toronto, 60 St George Street, Toronto, ON M5S 3H8, Canada

<sup>2</sup>University of Kentucky, Department of Physics and Astronomy, 177 CP Building, Lexington, KY 40506–0055, USA

<sup>3</sup>University of Calgary, 2500 University Dr NW, Calgary, AB T2N 1N4, Canada

Accepted 2004 February 11. Received 2004 February 6; in original form 2003 December 12

## ABSTRACT

Ever since the pioneering study of Spitzer, it has been widely recognized that grains play an important role in the heating and cooling of photoionized environments. This includes the diffuse interstellar medium and H II regions, planetary nebulae and photodissociation regions. A detailed code is necessary to model grains in a photoionized medium since the interactions of grains with their environment include a host of microphysical processes. In this paper we will use the spectral synthesis code CLOUDY for this purpose. A comprehensive upgrade of the grain model has been recently incorporated into CLOUDY. One of these upgrades is the newly developed hybrid grain charge model. This model allows discrete charge states of very small grains to be modelled accurately, while simultaneously avoiding the overhead of fully resolving the charge distribution of large grains, thus making the model both accurate and computationally efficient. A comprehensive comparison with the fully resolved charge state models of Weingartner & Draine shows that the agreement is very satisfactory for realistic size distributions. The effect of the grain size distribution on the line emission from photoionized regions is studied by taking standard models for an H II region and a planetary nebula and adding a dust component to the models with varying grain size distributions. A comparison of the models shows that varying the size distribution has a dramatic effect on the emitted spectrum. The strongest enhancement is always found in optical/UV lines of the highest ionization stages present in the spectrum (with factors up to 2.5–4), while the strongest decrease is typically found in optical/UV lines of low ionization lines or infrared fine-structure lines of low/intermediate ionization stages (with reductions up to 10–25 per cent). Changing the grain size distribution also affects the ionization balance, and can affect resonance lines which are very sensitive to changes in the background opacity. All these results clearly demonstrate that the grain size distribution is an important parameter in photoionization models.

**Key words:** plasmas – methods: numerical – circumstellar matter – dust, extinction – H II regions – planetary nebulae: general.

## 1 INTRODUCTION

Grains are ubiquitous in the interstellar medium (ISM), and they can be detected either directly through their far-infrared emission or indirectly through extinction or polarization studies. Despite the vast number of observations, many questions regarding grain com-

position and grain physics remain unanswered. Further study is therefore required, and detailed models are needed to interpret the results. Ever since the pioneering study of Spitzer (1948), it has been widely recognized that grains play an important role in the heating and cooling of the diffuse ISM (see also the more recent studies by Bakes & Tielens 1994; Weingartner & Draine 2001a, hereafter WD). Grains also play an important role in the physics of H II regions and planetary nebulae (PNe; e.g. Maciel & Pottasch 1982; Baldwin et al. 1991, hereafter BFM, Borkowski & Harrington 1991; Ercolano et al. 2003) and photodissociation regions (PDRs; e.g. Tielens & Hollenbach 1985).

The interactions of grains with their environment include a host of microphysical processes, and their importance and effects can only be judged by including all of these processes in a self-consistent

\*E-mail: p.van-hoof@qub.ac.uk

†Current address: Queen’s University Belfast, Physics Department, APS Division, Belfast BT7 1NN.

‡Current address: The Department of Physics and Astronomy, George Mason University, 4400 University Drive, MSN 3F3, Fairfax, VA 22030, USA.

§Current address: Gemini Observatory, Southern Operations Centre, Colina el Pina S/N, La Serena, Chile.

manner. This can, in turn, only be performed with a complete simulation of the environment. In this paper we use the spectral synthesis code CLOUDY for this purpose. CLOUDY is a well-known and widely used photoionization code. This code is not only useful for modelling fully ionized regions, but calculations can also be continued into the PDR. In order to make the models realistic, the presence of a detailed grain model is usually required. The first grain model was introduced into CLOUDY in 1990 to facilitate more accurate modelling of the Orion nebula (for a detailed description see BFM). In subsequent years, this model has undergone some revisions and extensions, but remained largely the same.

In the last couple of years, CLOUDY has undergone several major upgrades, described in Ferland (2000a), Ferland (2000b) and van Hoof, Martin & Ferland (2000b). This includes a comprehensive upgrade of the grain model. The latter was necessary for two reasons. First, the discovery of crystalline silicates in stellar outflows (e.g. Waters et al. 1996), and other detailed observations of grain emission features by the *Infrared Space Observatory* (ISO), meant that the code had to become much more flexible to allow such materials to be included in the modelling. Secondly, even before the ISO mission it had already become clear that the photoelectric heating and collisional cooling of the gas surrounding the grains is dominated by very small grains (possibly consisting of polycyclic aromatic hydrocarbons or PAHs). The physics of very small grains could not be modelled very accurately with the original grain model. In view of these facts we have undertaken a comprehensive upgrade of the grain model in CLOUDY. The two main aims were to make the code more flexible and versatile, and to make the modelling results more realistic (e.g. by improving the treatment of grain charging, the photoelectric effect, and stochastic heating). The new grain model has been introduced in version 96 of CLOUDY.

We have used a three-pronged approach to improve the grain model in CLOUDY. First, we introduced a Mie code for spherical particles, which allows the user to use arbitrary grain materials and resolve any grain size distribution of their choosing to arbitrary precision. The latter is very important since most grain properties depend strongly (and more importantly non-linearly) on size. This upgrade, briefly described in Section 2, also opened the way for two other major improvements. First, it enabled the accurate modelling of stochastic heating effects for arbitrary grain materials and size distributions. Secondly, it enabled a much more realistic modelling of grain charging, photoelectric heating, and collisional cooling by the grains, as described in Section 3. For this purpose we have developed a completely new grain charge model, which we call the hybrid model. This is described in detail in Section 3.1.

In this paper we will study photoelectric heating by grains in photoionized environments in detail. In particular, we will study the effect that the distribution of grain sizes has on the relative intensities of emission lines. We will show that this effect is nothing short of dramatic, making the grain size distribution an important parameter in the modelling of photoionized regions such as H II regions and planetary nebulae. This will be described in Section 4. Our conclusions will be summarized in Section 5.

## 2 RESOLVING THE GRAIN SIZE DISTRIBUTION

In the original grain model of CLOUDY, opacities for a handful of grain species were hard-wired in the code. Furthermore, all grain properties would be integrated or averaged over the entire size distribution. This is not a very good approximation since most of these

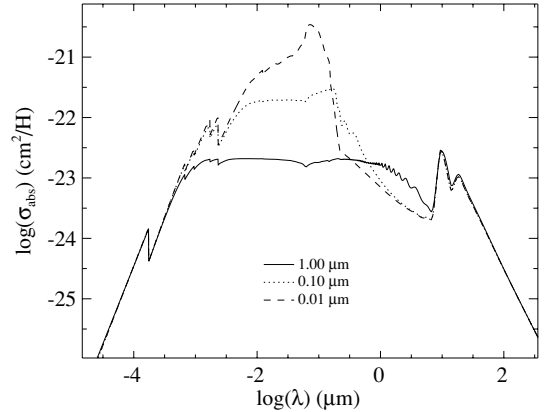


**Figure 1.** The absorption cross-section for astronomical silicate (Martin & Rouleau 1991) for three single sized grains. The dust-to-gas ratio is the same for all three species and the cross-sections are normalized per hydrogen nucleus in the plasma.

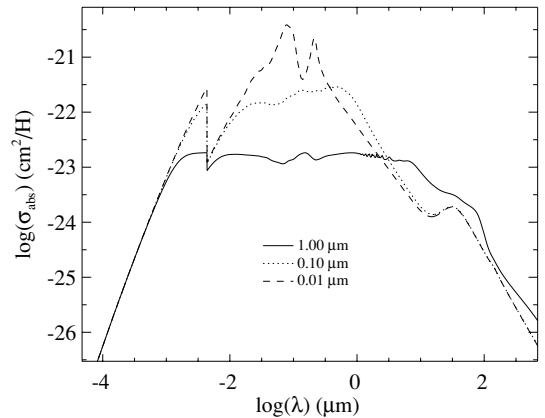


**Figure 2.** Same as in Fig. 1, but for graphite (Martin & Rouleau 1991).

properties depend strongly on size. This approach was nevertheless adhered to in BFM because of computational restrictions.

Resolving the size distribution into many small bins improves the modelling in several ways. First, the absorption cross-sections of small grains are very different from large grains (see Figs 1 and 2). Resolving the size distribution into many size bins enables the equilibrium temperature to be calculated for each bin separately. This leads to a more accurate prediction for the spectrum since grain emissions are a strongly non-linear function of temperature.

More importantly, resolving the size distribution also enables other improvements of the grain treatment: stochastic heating can be treated correctly for the smallest grains in the size distribution (this will be discussed in more detail in a forthcoming paper), and the calculations yield much more accurate results for grain charging, photoelectric heating and collisional cooling of the gas by the grains (see Section 3).

To improve the model, we have implemented the following changes.

(i) We have included a Mie code for spherical particles in CLOUDY. Assuming that the grains are homogeneous spheres with a given complex refractive index (optical constant) one can use Mie theory (Mie 1908) to calculate the absorption and scattering opacity. This has to be performed separately for every wavelength since the

refractive index depends on wavelength. Good overviews of Mie theory can be found in van de Hulst (1957) and Bohren & Huffman (1983). Our Mie code is based on the program outlined in Hansen & Travis (1974) and references therein. The optical constants needed to run the code are read from a separate file. This allows greater freedom in the choice of grain species. Files with optical constants for a range of materials are included in the CLOUDY distribution. However, the user can also supply optical constants for a completely different grain type.

(ii) Several mixing laws have been included in the code (Brugge-man 1935; Stognienko, Henning & Ossenkopf 1995; Voshchinnikov & Mathis 1999, based on theory described in Farafonov 2000). This allows the user to define grains which are mixtures of different materials. CLOUDY will then calculate the appropriate opacities by combining the optical constants of these grain types.

(iii) It is possible to use arbitrary grain size distributions. The user can either choose one of a range of preset functions (with numerous free parameters), or supply the size distribution in the form of a table. Single-sized grains can also be treated.

(iv) The size distribution can be resolved in an arbitrary number of size bins (set by the user), and the absorption and scattering opacities and all the physical parameters (charge, temperature, etc.) are calculated for each bin separately.

### 3 CHANGES TO THE GRAIN PHYSICS

We have modified certain aspects of the grain physics following the discussion in WD. Below we highlight certain aspects of these changes. A detailed description will be presented in a forthcoming paper.

(i) We include the bandgap between the valence and conduction bands in our potential well model for silicates. This change only affects the results for negatively charged grains ( $Z_g \leq -1$ ).

(ii) Reduction of the potential barrier for negatively charged grains is included using an analytic fit to numerical calculations. Two effects are important here: quantum tunnelling and the Schottky effect. Quantum theory predicts that an electron with insufficient energy to overcome a barrier still has a finite chance of tunnelling through. This effect has been modelled using the WKB approximation which gives a simple analytic expression for the tunnelling probability for a barrier of given width and height. Quantum tunnelling is only important for small grains. For large grains the Schottky effect will dominate, which describes the lowering of the potential barrier by an image potential in the grain. This effect has been accurately modelled by Draine & Sutin (1987).

We will approximate both effects by assuming that the barrier is effectively reduced in height from  $-(Z_g + 1)e^2/(4\pi\epsilon_0 a)$  to  $-E_{\min}$ . The magnitude of the combined tunnelling/Schottky effect was calculated by WD. However, the fitting function they used has the wrong limiting behaviour for large grains where it should asymptotically approach the classical Schottky expression. We therefore repeated these calculations using the same assumptions, but adopted a different fitting function that does exhibit the correct limiting behaviour:

$$E_{\min} = -\theta_v \frac{e^2}{4\pi\epsilon_0 a} \left[ 1 - \frac{0.3}{(a/\text{nm})^{0.45} \nu^{0.26}} \right], \quad (1)$$

where  $\theta_v [\nu = -(Z_g + 1)]$  describes the Schottky effect and is defined in Draine & Sutin (1987). The term in square brackets describes the quantum-mechanical correction. This change only affects the results for grains with  $Z_g < -1$ .

(iii) The treatment of the photoelectric effect has been improved, following the discussion in WD. This includes new expressions for the ionization potential, photoelectric yield, and the energy distribution of ejected electrons.

(iv) Certain physical constants have been updated. Most notably, the work function for graphite has been lowered. The old value was equal to that of silicate, which was unrealistically high. The change results in an increased photoelectric heating rate.

(v) The treatment of electron sticking probabilities has been updated, again following WD. Especially for very small grains the sticking efficiency has been substantially lowered to obtain better agreement with laboratory studies of molecules. This has an important impact on the photoelectric heating rate of the gas since the electron recombination rate has to be matched by electron loss processes to preserve the charge balance. The loss processes are usually dominated by the photoelectric effect. We also introduced a minimum charge for the grains, as outlined in WD. This modification is relevant for very small grains in fully molecular regions. This change can have an important effect on the amount of free electrons and on the amount of heating from photodetachment.

(vi) The treatment of collisional processes between charged particles and the grains have been improved. The modification factors for Coulomb attraction or repulsion of incoming particles have been upgraded following Draine & Sutin (1987) who include image potential effects in the grains. We have also modified the physics for charge exchange between ions and grains. The new code is based on the assumption that electrons move into the deepest potential well, either the grain or the ion. In certain circumstances this may be different from the old assumption that ions always recombine to their neutral state upon impact. This change has little direct impact on the heating and cooling rates, but it can influence the grain charging and the ionization balance in the gas. In turn this can influence photoelectric heating rates.

Our treatment deviates from the WD code in two ways. Most importantly, we use a different grain charge model, which will be discussed in more detail in Section 3.1. Secondly, we use slightly different physics for charge exchange between ions and grains, as outlined above in point vi. The latter only gives rise to very small differences at the 1–2 per cent level or better when compared with the WD treatment.

#### 3.1 The new hybrid grain charge model

The original grain model in CLOUDY (which we will call the average grain potential model) is described in BFM. In that model an average grain potential is calculated by finding the potential for which the charge gain rate exactly matches the loss rate. This method was first proposed by Spitzer (1948), and is an excellent approximation for large grains. However, it is now clear that photoelectric heating and collisional cooling of the gas are dominated by very small grains. For such grains the average grain potential approximation does not work very well because grain physics becomes increasingly non-linear as a function of charge for smaller grain sizes. This fact, combined with the fact that grain charges are quantized, has led to a new approach where the charge distribution is fully resolved, and heating and cooling rates are calculated for each charge state separately (see, e.g., WD). This ensures accurate results, but leads to an appreciable increase in computational overhead. This is especially the case for large grains since the width of the charge distribution increases with grain size. Hence the paradoxical situation arises that most of the computing time is spent on grains which contribute least to heating



and cooling, and which are also the grains for which the average grain potential model works best!

In this paper we present a hybrid grain potential model which is almost as computationally efficient as the original average grain potential model, but nevertheless gives sufficient accuracy when compared with fully resolved charge distribution calculations. The basic philosophy is that for very small grains ( $a < 1$  nm) only a few charge states have a significant population. Hence we adopt the  $n$ -charge state approximation, in which all grains are treated by using exactly  $n$  contiguous charge states, independent of size. The higher  $n$  is, the more accurate the results will be (exactly how accurate will be discussed in Section 3.2). The default for CLOUDY calculations is  $n = 2$ , but the user can request a larger number if higher precision is desired.

Since the  $n$ -charge state model does not fully resolve the charge distribution, a different algorithm from WD is needed to calculate the charge states  $Z_i \equiv Z_1 + i - 1$ , and the population of these states. The value of the lowest of the  $n$  grain charges,  $Z_1$ , is found using an iterative procedure, as discussed below. The populations  $f_i$  of the charge states must first of all obey the following normalization:

$$\sum_{i=1}^n f_i = 1. \quad (2)$$

Secondly, we require that the electron gain rates  $J_i^-$  and electron loss rates  $J_i^+$  summed over all charge levels match exactly:

$$\sum_{i=1}^n f_i (J_i^+ - J_i^-) = 0, \quad (3)$$

similar to the average grain potential model.  $Z_1$  is defined by requiring that  $J_i^+ - J_i^-$  changes sign between  $Z_1$  and  $Z_2$  when  $n = 2$ . Equations (2) and (3) are sufficient to determine the charge state populations if  $n = 2$ , but for  $n > 2$  we need additional equations. These equations need to satisfy the following constraints. First, the resulting level populations should always be greater or equal to zero. Secondly, the level populations should change continuously when the electron gain and loss rates change continuously. Thirdly, the level populations should asymptotically approach the results from fully resolved calculations for increasing values of  $n$ . We have adopted the following algorithm.

(i) The  $n$  charge states are split up in two groups of  $n - 1$  contiguous charge states. The first group contains charge states  $[Z_1, Z_{n-1}]$ , and the second  $[Z_2, Z_n]$ . The value for  $Z_1$  is determined iteratively (see step iv).

(ii) The relative level populations in the first group  $f_i^1$  are determined using an algorithm very similar to the one used in fully resolved calculations, i.e. assume  $f_1^1 = 1$ , calculate  $f_2^1 = f_1^1 J_1^+ / J_2^-$ ,  $f_3^1 = f_2^1 J_2^+ / J_3^-$ , etc.<sup>1</sup> and then re-normalize to  $\sum_{i=1}^{n-1} f_i^1 = 1$ . We use an analogous procedure for the populations  $f_i^2$  of the second group for  $i \in [2, n]$ .

(iii) Determine for both groups the net charging rate

$$J_k = \sum_{i=k}^{n-2+k} f_i^k (J_i^+ - J_i^-) \quad (k = 1, 2). \quad (4)$$

<sup>1</sup> Note that this procedure is not correct for charge transfer with multiply charged ions. In order to avoid having to solve a full set of linear equations, we will approximate this process as multiple single-charge-transfer events. The resulting errors are expected to be small as collision rates for multiply charged ions are usually quite low because their velocities are small compared with electrons. The collision rates are normally suppressed even further by the positive grain charge.

(iv) Iterate  $Z_1$  and repeat steps 1–3 until  $J_1 \times J_2 \leq 0$ . Then find  $0 \leq \alpha \leq 1$  such that

$$\alpha J_1 + (1 - \alpha) J_2 = 0. \quad (5)$$

(v) Determine the final charge state populations as follows:

$$f_i = \alpha f_i^1 + (1 - \alpha) f_i^2 \quad (\text{with } f_n^1 \equiv 0, f_1^2 \equiv 0). \quad (6)$$

One can verify that this algorithm satisfies all constraints.

The hybrid grain potential model is efficient because it avoids the overhead for large grains, while still giving accurate results for both small and large grains. An added bonus is that most of the time an excellent initial estimate for  $Z_1$  can be derived from the previous zone, reducing the overhead even further. The model works for very small grains because only few charge states are populated and it can reconstruct the actual charge distribution. It works for large grains because the grain potential distribution approaches a delta function for increasing grain size (as opposed to the charge distribution which becomes ever wider). Our method therefore asymptotically approaches the average grain potential model, which we already know is very accurate for large grains. No simple predictions can be made as to how the hybrid grain charge model will behave for intermediate grain sizes. We therefore conducted comprehensive tests which will be discussed in Section 3.2.

### 3.2 Validating the hybrid grain charge model

In order to validate the new grain charge model, we calculated the photoelectric heating and collisional cooling rates for a range of physical conditions, two grain species, and a wide range of grain sizes (including a realistic size distribution). We modelled conditions typical for the warm and cold ISM, H II regions (both the ionized region and the PDR surrounding it), and planetary nebulae (again both the ionized region and the PDR). We modelled the physical conditions with simple assumptions: the plasma only contained hydrogen, the electron temperature and density were fixed at prescribed values, and the incident spectrum was assumed to be a blackbody (either full in the warm ISM and ionized cases, or cut-off at 13.6 eV in the cold ISM and PDR cases). The physical parameters are summarized in Table 1. The grain materials were assumed to be astronomical silicate and graphite (Draine & Lee 1984), and the grain size distribution was the A6 case with  $R_V = 3.1$  taken from Weingartner & Draine (2001b). We then compared these calculations with benchmark results from the WD code, which fully resolves the charge distribution. A detailed discussion of these tests (including tables of photoelectric heating and collisional cooling rates) can be found in van Hoof et al. (2001).

In Table 2 we summarize the comparison of the photoelectric heating and collisional cooling rates from van Hoof et al. (2001).

**Table 1.** Physical parameters for the benchmark models. Symbols have their usual meaning,  $G$  is the intensity of the radiation field and  $G_0 = 1.6 \times 10^{-6} \text{ W m}^{-2}$ , integrated between 6 and 13.6 eV, is the Habing intensity.  $T_c$  is the colour temperature of the radiation field.

|                                     | ISM  |      | H II    |     | PN      |     |
|-------------------------------------|------|------|---------|-----|---------|-----|
|                                     | Warm | Cold | Ionized | PDR | Ionized | PDR |
| $T_c/\text{kK}$                     | 35   | 35   | 50      | 50  | 250     | 250 |
| $\log(G/G_0)$                       | 0    | 0    | 5       | 5   | 5       | 5   |
| $\log(n_{\text{H}}/\text{cm}^{-3})$ | 0    | 1    | 4       | 4   | 4       | 4   |
| $\log(n_e/\text{cm}^{-3})$          | 0    | -2   | 4       | 1   | 4       | 1   |
| $T_c/\text{kK}$                     | 9    | 0.1  | 9       | 1   | 20      | 1   |

**Table 2.** Summary of the comparison of photoelectric heating rates and collisional cooling rates between the CLOUDY  $n$ -charge state calculations (indicated by CLD $n$ ) and the benchmark calculations with the WD code. All entries are differences CLD $n$ /WD  $-1$  in per cent.

|      | Heating     |       |                   |       |
|------|-------------|-------|-------------------|-------|
|      | Single size |       | Size distribution |       |
|      | Median      | Worst | Median            | Worst |
| CLD2 | -3.03       | -55.5 | -9.85             | -23.1 |
| CLD3 | -2.44       | -29.9 | -8.34             | -16.3 |
| CLD4 | -1.40       | -9.6  | -3.43             | -4.7  |
| CLD5 | -0.75       | -5.9  | -1.45             | -2.8  |
|      | Cooling     |       |                   |       |
|      | Single size |       | Size distribution |       |
|      | Median      | Worst | Median            | Worst |
| CLD2 | -0.77       | -23.1 | -3.05             | -3.7  |
| CLD3 | -0.72       | -12.5 | -2.27             | -3.5  |
| CLD4 | -0.65       | +5.2  | -1.30             | -3.1  |
| CLD5 | -0.44       | +3.5  | -1.21             | -2.7  |

**Table 3.** Comparison of the fractional charge state populations, average charge and photoelectric heating rates of a 5-Å silicate grain in cold ISM conditions resulting from the WD and  $n$ -charge state calculations. The results from the 5-charge state calculations are omitted since they are virtually identical to the 4-charge state results. Entries  $a(-b)$  stand for  $a \times 10^{-b}$ .

| $Z/e$               | Fractional charge state populations              |           |           |           |
|---------------------|--------------------------------------------------|-----------|-----------|-----------|
|                     | WD                                               | CLD2      | CLD3      | CLD4      |
| -1                  | 0.1271                                           | -         | 0.0594    | 0.1272    |
| 0                   | 0.8325                                           | 0.9876    | 0.9152    | 0.8326    |
| 1                   | 0.0404                                           | 0.0124    | 0.0254    | 0.0402    |
| 2                   | 9.94(-6)                                         | -         | -         | 4.97(-9)  |
| $\langle Z \rangle$ | Average charge in e                              |           |           |           |
|                     | WD                                               | CLD2      | CLD3      | CLD4      |
|                     | -0.0866                                          | +0.0124   | -0.0340   | -0.0870   |
| $Z/e$               | Photoelectric heating rates in $\text{W m}^{-3}$ |           |           |           |
|                     | WD                                               | CLD2      | CLD3      | CLD4      |
| -1                  | 2.51(-27)                                        | -         | 1.17(-27) | 2.50(-27) |
| 0                   | 1.53(-27)                                        | 1.80(-27) | 1.66(-27) | 1.51(-27) |
| 1                   | 1.27(-31)                                        | 3.61(-32) | 7.40(-32) | 1.17(-31) |
| 2                   | 0.00                                             | -         | -         | 0.00      |

These tables show the relative discrepancy between the WD and CLOUDY results in per cent. In general, the results are in excellent agreement, with only a few outliers for single sized grains in the  $n = 2$  and 3 cases. The origin of these discrepancies is studied in more detail for the worst performing single sized grain in both the  $n = 2$  and 3 cases: a 5-Å silicate grain in cold ISM conditions. The charge state populations from the WD and CLOUDY models are compared in the top panel of Table 3. The  $n$ -charge state model was designed to find the charge distribution, and hence one would expect that the average charge should be in reasonable agreement with fully resolved calculations. The middle panel of Table 3 shows that this is indeed the case. Key to understanding the discrepancy in the photoelectric heating rates is the observation that these rates behave

non-linearly as a function of charge, and that the rates are highest for the lowest charge states. The non-linearity is strongest for very small grains close to their lowest allowed charge state ( $Z = -1$  for the 5-Å silicate grain). This is illustrated in the bottom panel of Table 3: the  $Z = -1$  state produces more than 62 per cent of the photoelectric heating, while less than 13 per cent of the grains are in that charge state. Since the  $n = 2$  calculations produce an average charge slightly above zero, the model is missing the  $Z = -1$  state which would have given the largest contribution to the photoelectric heating. This also explains why the photoelectric heating rates from the  $n$ -charge state model are consistently lower than the WD results, although they do asymptotically approach the correct result for larger grain size or larger  $n$ . When  $n$  is not high enough to fully resolve the charge state distribution, the photoelectric heating from the lowest charge states will be missed. Even the increased population of some of the higher states cannot fully make up for that loss and the total amount of heating will be somewhat underestimated.

The results for the size distribution cases always agree to better than 25 per cent, even for  $n = 2$ . The worst-case performance is found in PDR type conditions where grains tend to be negative, while in ionized regions the results agree to better than 8 per cent. This is well within the accuracy with which we know grain physics to date. There are still major uncertainties in the photoelectric yields and the sticking efficiency for electrons, both of which have a strong effect on the photoelectric heating rate. Also the work function and bandgap for astrophysical grain materials are poorly known and can have a strong effect as well. This is unfortunate since photoelectric heating and collisional cooling in photoionized environments are important effects. These uncertainties largely stem from our uncertain knowledge of the composition of interstellar grains.

From the bottom panel of Table 2 one can see that the collisional cooling rates are usually in better agreement than the photoelectric heating rates for a given set of physical parameters. Furthermore, it is clear that the accuracy of the  $n$ -charge state approximation increases as  $n$  increases, as should be expected. Closer inspection of Tables 2–4 from van Hoof et al. (2001) for single sized grains reveals that the largest errors in the  $n = 2$  and 3 cases are for the 0.5 nm grains, for  $n = 4$  for either 2 or 10 nm grains, and for  $n = 5$  for 10 nm grains, i.e. the grain size for which the errors are largest shifts upwards for higher values of  $n$ . This is expected since the  $n$ -charge state approximation will fully resolve the charge distribution of the smallest grains for  $n > 3$ . Note that the results for the 100 nm grains are always in excellent agreement, even when  $n = 2$ , despite the fact that the actual charge distribution is much wider than that.

The agreement between the CLOUDY and the WD results is very satisfactory for realistic size distributions, and should be sufficient for all realistic astrophysical applications. Therefore, the hybrid grain charge model presented above (with  $n = 2$ ) will be the default for CLOUDY modelling. By issuing a simple command, the user can choose a higher value for  $n$  if higher precision is desired. The default value for  $n$  will be increased in the near future when greater computer speed and/or greater efficiency of the algorithm will allow us to do so. We will use  $n = 2$  below for a more detailed study of the photoelectric heating effect in dusty ionized plasmas.

## 4 PHOTOELECTRIC HEATING IN IONIZED REGIONS

### 4.1 Introduction

An energetic electron can be ejected from a grain following the absorption of a photon. The photoelectrons share their energy with the

**Table 4.** Properties of the grains included in the models. For size distributions where no distinction is made between the silicate and the graphite component (single sized grains, MRN, and KMH), the entry is equally valid for both materials. The total dust-to-gas mass ratio is  $6.34 \times 10^{-3}$  for the H II-region models,  $3.96 \times 10^{-3}$  for the PN models containing silicate grains, and  $2.34 \times 10^{-3}$  for the PN models containing graphite.

| No.                                | Label                      | $R_V$ | $a_{\min}$<br>( $\mu\text{m}$ ) | $a_{\max}$<br>( $\mu\text{m}$ ) | $n_{\text{bin}}$ |
|------------------------------------|----------------------------|-------|---------------------------------|---------------------------------|------------------|
| H II region models                 |                            |       |                                 |                                 |                  |
| 0                                  | no dust                    | –     | –                               | –                               | –                |
| 1                                  | 1.0 $\mu\text{m}$          | –     | 1.000 00                        | 1.0000                          | 1                |
| 2                                  | 0.1 $\mu\text{m}$          | –     | 0.100 00                        | 0.1000                          | 1                |
| 3                                  | MRN55 <sup>a</sup>         | 5.5   | 0.030 00 <sup>d</sup>           | 0.2500                          | 9                |
| 4                                  | KMH53 <sup>b</sup>         | 5.3   | 0.002 50                        | 3.0000                          | 31               |
| 5                                  | WD55 A0 (sil) <sup>c</sup> | 5.5   | 0.000 35                        | 0.4186                          | 31               |
|                                    | WD55 A0 (gra) <sup>c</sup> | 5.5   | 0.000 35                        | 4.2102                          | 41               |
| 6                                  | WD55 A3 (sil) <sup>c</sup> | 5.5   | 0.000 35                        | 0.4145                          | 31               |
|                                    | WD55 A3 (gra) <sup>c</sup> | 5.5   | 0.000 35                        | 1.6662                          | 62               |
| Planetary nebula models (silicate) |                            |       |                                 |                                 |                  |
| 0                                  | no dust                    | –     | –                               | –                               | –                |
| 1                                  | 1.0 $\mu\text{m}$          | –     | 1.000 00                        | 1.0000                          | 1                |
| 2                                  | 0.1 $\mu\text{m}$          | –     | 0.100 00                        | 0.1000                          | 1                |
| 3                                  | WD31 A0 <sup>c</sup>       | 3.1   | 0.000 35                        | 0.3852                          | 30               |
| 4                                  | WD31 A6 <sup>c</sup>       | 3.1   | 0.000 35                        | 0.3805                          | 30               |
| 5                                  | MRN31 <sup>a</sup>         | 3.1   | 0.005 00                        | 0.2500                          | 17               |
| 6                                  | KMH31 <sup>b</sup>         | 3.1   | 0.002 50                        | 3.0000                          | 31               |
| Planetary nebula models (graphite) |                            |       |                                 |                                 |                  |
| 0                                  | no dust                    | –     | –                               | –                               | –                |
| 1                                  | 1.0 $\mu\text{m}$          | –     | 1.000 00                        | 1.0000                          | 1                |
| 2                                  | 0.1 $\mu\text{m}$          | –     | 0.100 00                        | 0.1000                          | 1                |
| 3                                  | MRN31 <sup>a</sup>         | 3.1   | 0.005 00                        | 0.2500                          | 17               |
| 4                                  | WD31 A0 <sup>c</sup>       | 3.1   | 0.000 35                        | 1.3399                          | 38               |
| 5                                  | KMH31 <sup>b</sup>         | 3.1   | 0.002 50                        | 3.0000                          | 31               |
| 6                                  | WD31 A6 <sup>c</sup>       | 3.1   | 0.000 35                        | 1.0222                          | 60               |

<sup>a</sup>Mathis, Rumpl & Nordsieck (1977). <sup>b</sup>Kim, Martin & Hendry (1994). <sup>c</sup>Weingartner & Draine (2001b). <sup>d</sup>The Mathis et al. (1977) size distribution was truncated at a lower limit of 0.03  $\mu\text{m}$  to simulate the grain size distribution in Orion. See also the discussion in BFM.

gas via collisions, raising the local electron temperature; this process is known as photoelectric heating. This excess energy can then be used to enhance collisional excitation of certain (usually forbidden) emission lines, which will change the emitted spectrum. This effect is known and has been described in Dopita & Sutherland (2000) and Volk (2001). The photoelectric effect will also alter the ionization balance in the plasma. In a typical photoionized plasma the free electrons will not have enough energy for collisional ionization to be an important process. However, the raise in electron temperature will reduce the recombination rates and thereby lead to an overall increase in ionization. All of these processes are known. However, it is not widely known that the size distribution of the grains plays a very important role in determining the magnitude of this effect.

#### 4.2 Description of the models

In order to test this, we have constructed a set of models with CLOUDY 96 BETA 5 based on the standard Paris H II region and planetary nebula models (HII40 and PN150, respectively, Péquignot et al. 2001). The Paris H II region model is valid for low-excitation photoionized gas, while the Paris PN model is valid for high-excitation gas. The base models contain no dust, and will be used as a point of reference. We constructed six models out of each base model by simply adding a dust component. Two models adopt single sized grains of 1.0 and

0.1  $\mu\text{m}$ , while the other four adopt more or less realistic size distributions taken from the literature, as indicated in Table 4. These size distributions were all constructed for the purpose of reproducing interstellar extinction curves. They were used in our models because they are the most detailed studies of grain size distributions that can be found in the literature. In order to keep the models plausible, we used size distributions that reproduce the  $R_V = 5.5$  extinction curve for the H II region models, and size distributions that reproduce the  $R_V = 3.1$  extinction curve for the PN models. For the H II region model we used a mixture of silicates and graphite (Martin & Rouleau 1991) with a dust-to-gas mass ratio of  $6.34 \times 10^{-3}$ . In the planetary nebula cases, we made separate models for either silicate or graphite (with a dust-to-gas mass ratio of  $3.96 \times 10^{-3}$  and  $2.34 \times 10^{-3}$ , respectively) as these two species are not expected to coexist spatially in the nebular material on theoretical grounds.<sup>2</sup> Note that the size distributions presented in Weingartner & Draine (2001b) were derived by matching the extinction curve using grain opacities defined in Li & Draine (2001). In this study we use the same size distribution, but use graphite opacities from Martin & Rouleau (1991) instead, which is not consistent. This inconsistency is irrelevant for our purposes; more detailed studies will have to await the construction of realistic size distributions for H II regions and planetary nebulae. In all cases the size distribution was resolved to a precision  $\ln(a_{n+1}/a_n) \approx 0.23$ . This resolution is sufficient to accurately converge the effects of the grains. The resulting number of size bins, together with the lower and upper limit of the size range, is indicated in Table 4. We stress that in all comparisons the chemical composition and the dust-to-gas mass ratio of the dust is the same, and the only difference is the size distribution. We also point out that the models are ionization bounded, so the outer radius varies, depending on the total opacity of the grains (which also depends strongly on the size distribution). Since the grains and the atomic gas are competing for ionizing photons, this also creates a mild dependence of the overall ionization structure on the size distribution of the grains.

#### 4.3 Results and discussion

In Tables 5–7 we present the results of these calculations. These tables contain a comparison of the flux (presented as a ratio to  $H\beta = 1$  for that particular model) of the most important infrared fine-structure lines, as well as optical and UV emission lines. A number of physical parameters are also compared, such as the total  $H\beta$  flux, the electron temperature at the inner edge of the nebula and the volume average over the entire nebula, the fractional ionization of helium (given as the ratio of the ion abundance over the total helium abundance), the outer radius, and the fraction that the photoelectric heating and collisional cooling contribute to the total heating and cooling of the gas.

The WD55 A3 and WD31 A6 size distributions contain enhanced amounts of very small carbonaceous particles (PAHs). Such particles are not expected to exist in ionized regions, and hence the models with graphite based on these size distributions are less realistic than those based on other size distributions. In the following

<sup>2</sup> Note that spectroscopy of planetary nebulae by ISO has revealed a surprisingly large number of cases that show both silicate and graphitic dust features. One famous example is NGC 6302 (Molster et al. 2001). It is, however, usually assumed that the two species reside in different parts of the nebula.



**Table 5.** Results for the H II region models. The line flux ratio relative to  $H\beta = 1$  is given for the most important emission lines in the model and certain relevant physical quantities such as the total  $H\beta$  flux, the electron temperature, helium ionization fractions, the outer radius, the continuum optical depth at 121.6 nm, and the fraction of the total gas heating and cooling contributed by the grains. Quantities between angled brackets are volume averages over the entire ionized region.

| Model label<br>Model no.                                           | None<br>0 | 1.0 $\mu\text{m}$<br>1 | 0.1 $\mu\text{m}$<br>2 | MRN55<br>3 | KMH53<br>4 | WD55 A0<br>5 | WD55 A3<br>6 |
|--------------------------------------------------------------------|-----------|------------------------|------------------------|------------|------------|--------------|--------------|
| He I 587.6 nm                                                      | 0.1181    | 0.1167                 | 0.1203                 | 0.1229     | 0.1301     | 0.1316       | 0.1353       |
| C II] 232.6 nm                                                     | 0.1995    | 0.2020                 | 0.2123                 | 0.2137     | 0.2141     | 0.2137       | 0.2041       |
| C III] 190.9 nm                                                    | 0.0533    | 0.0538                 | 0.0862                 | 0.1009     | 0.1673     | 0.2162       | 0.4784       |
| [N II] 658.4 nm                                                    | 0.5331    | 0.5423                 | 0.5335                 | 0.5188     | 0.4703     | 0.4586       | 0.4247       |
| [N II] 121.7 $\mu\text{m}$                                         | 0.0281    | 0.0286                 | 0.0269                 | 0.0257     | 0.0219     | 0.0210       | 0.0184       |
| [N III] 57.32 $\mu\text{m}$                                        | 0.2981    | 0.2950                 | 0.3183                 | 0.3292     | 0.3641     | 0.3776       | 0.4162       |
| [O II] 372.7 nm                                                    | 2.0913    | 2.1158                 | 2.2401                 | 2.2578     | 2.3174     | 2.3633       | 2.4778       |
| [O III] 500.7 nm                                                   | 1.5023    | 1.5172                 | 2.0366                 | 2.2263     | 2.9554     | 3.4175       | 5.0999       |
| [O III] 51.80 $\mu\text{m}$                                        | 1.2139    | 1.1991                 | 1.2755                 | 1.3179     | 1.4505     | 1.4979       | 1.6344       |
| [O III] 88.33 $\mu\text{m}$                                        | 1.1114    | 1.1074                 | 1.2076                 | 1.2525     | 1.3953     | 1.4523       | 1.6240       |
| [Ne II] 12.81 $\mu\text{m}$                                        | 0.1765    | 0.1774                 | 0.1739                 | 0.1699     | 0.1574     | 0.1540       | 0.1424       |
| [Ne III] 386.9 nm                                                  | 0.0583    | 0.0590                 | 0.0842                 | 0.0942     | 0.1344     | 0.1610       | 0.2659       |
| [Ne III] 15.55 $\mu\text{m}$                                       | 0.2924    | 0.2886                 | 0.3120                 | 0.3255     | 0.3697     | 0.3870       | 0.4401       |
| [S II] 672.0 nm                                                    | 0.1555    | 0.1579                 | 0.1715                 | 0.1724     | 0.1694     | 0.1704       | 0.1736       |
| [S III] 953.1 nm                                                   | 0.7860    | 0.7909                 | 0.8462                 | 0.8597     | 0.9135     | 0.9466       | 1.0397       |
| [S III] 18.71 $\mu\text{m}$                                        | 0.6214    | 0.6215                 | 0.6218                 | 0.6205     | 0.6194     | 0.6207       | 0.6227       |
| [S III] 33.47 $\mu\text{m}$                                        | 1.2270    | 1.2214                 | 1.2203                 | 1.2171     | 1.2113     | 1.2120       | 1.2115       |
| [S IV] 10.51 $\mu\text{m}$                                         | 0.5312    | 0.5315                 | 0.5876                 | 0.6130     | 0.6960     | 0.7340       | 0.8532       |
| $\log[F(H\beta)/\text{erg s}^{-1}]$                                | 37.302    | 37.291                 | 37.169                 | 37.139     | 37.086     | 37.065       | 36.979       |
| $T_e/K$ inner edge                                                 | 7517      | 7597                   | 8290                   | 8444       | 8805       | 9274         | 11 090       |
| $\langle T_e/K \rangle$                                            | 7998      | 8017                   | 8318                   | 8395       | 8670       | 8851         | 9462         |
| $\langle \text{He}^0/\text{He} \rangle$                            | 0.253     | 0.262                  | 0.215                  | 0.191      | 0.117      | 0.095        | 0.051        |
| $\langle \text{He}^+/\text{He} \rangle$                            | 0.746     | 0.738                  | 0.785                  | 0.809      | 0.883      | 0.904        | 0.948        |
| $R_{\text{out}}/10^{19}$ cm                                        | 1.442     | 1.431                  | 1.319                  | 1.292      | 1.252      | 1.239        | 1.186        |
| $\tau_{121.6}$                                                     | 0.107     | 0.154                  | 0.729                  | 0.903      | 0.668      | 0.655        | 0.626        |
| $\langle a^2 \rangle / \langle a^3 \rangle$ ( $\mu\text{m}^{-1}$ ) | –         | 1.00                   | 10.00                  | 11.55      | 15.33      | 27.54        | 112.95       |
| GrGH/TotH                                                          | 0.000     | 0.005                  | 0.059                  | 0.072      | 0.130      | 0.185        | 0.348        |
| GrGC/TotC                                                          | 0.000     | 0.0019                 | 0.019                  | 0.024      | 0.038      | 0.056        | 0.136        |

discussion, results pertaining to these models will only be included in parentheses.

The numbers in Tables 5–7 show that adding a dust component has a dramatic effect on the physical conditions and the normalized spectrum. In the H II region models the strongest enhancements in line strength (compared with the base model without dust) are for C III] 190.9 nm with a factor 4.06 enhancement for the WD55 A0 size distribution (WD55 A3: 8.98), followed by [Ne III] 386.9 nm with a factor 2.76 (4.56), and [O III] 500.7 nm with a factor 2.27 (3.39). The strongest decrease is for the [N II] 121.7- $\mu\text{m}$  line with a factor 0.747 (WD55 A3: 0.655), followed by [N II] 658.4 nm with a factor 0.860 (0.797) and [Ne II] 12.81  $\mu\text{m}$  with a factor 0.873 (0.807). For the PN models the lines with the strongest enhancement are O v] 121.8 nm with a factor 2.66 for silicate and 2.85 for graphite (WD31 A6: 3.41), followed by O vi] 103.2 nm with factors 2.30 for silicate and 2.40 (2.94) for graphite, and O iv] 140.2 nm with factors 2.07 for silicate and 2.32 (2.58) for graphite. The strongest decrease in the silicate models is for the He I 587.6 nm line with a factor 0.895, followed by [S IV] 10.51  $\mu\text{m}$  with a factor 0.933 and [O III] 51.80  $\mu\text{m}$  with a factor 0.946. The strongest decrease in the graphite models is for the He I 587.6 nm line with a factor 0.890 (WD31 A6: 0.868), followed by Mg II 279.8 nm with a factor 0.895 (0.926), and [S IV] 10.51  $\mu\text{m}$  with a factor 0.942 (0.930). The variation of the relative strength of these lines is also shown in Fig. 3.

What is apparent from this comparison is that the strongest enhancement is always found in optical/UV lines of the highest ioniza-

tion stages in the spectrum, while the strongest decrease is typically found in optical/UV lines of low ionization lines or infrared fine-structure lines of low/intermediate ionization stages. This indicates that the effect is strongest in the inner regions of the nebula. This is confirmed by comparing the electron temperature at the inner edge of the nebula and the average over the entire volume. It is clear that in all cases the former changes far more strongly than the latter. What is also clear from the comparison is that the enhancement in emission line strength correlates well with the total amount of photoelectric heating contributed to the plasma by the grains. This is no surprise since most of the emission lines (with the exception of the helium lines) are predominantly collisionally excited. Small grains contribute far more to photoelectric heating than large grains, due to their much higher opacities (see Figs 1 and 2) and photoelectric yields (see fig. 5 in WD). Thus, one can roughly state that the more small particles a size distribution contains, the stronger the photoelectric heating of the plasma by the grains will be, which in turn leads to a stronger effect on the emitted spectrum. The fact that this effect is strongest at the inner edge can be understood by looking at Figs 1 and 2. It is apparent that for the smallest grains the absorption opacity peaks at a wavelength that corresponds fairly well with the Lyman edge of hydrogen. This implies that at the inner edge the grains will absorb lots of ionizing photons. However, when one moves away from the illuminated face of the nebula, more and more ionizing photons will be absorbed away, while non-ionizing photons will be less affected. Since grains can absorb both,

**Table 6.** Same as Table 5, but for the planetary nebula region models with silicate.

| Model label                                                    | None   | 1.0 $\mu\text{m}$ | 0.1 $\mu\text{m}$ | WD31 A0 | WD31 A6 | MRN31  | KMH31  |
|----------------------------------------------------------------|--------|-------------------|-------------------|---------|---------|--------|--------|
| Model no.                                                      | 0      | 1                 | 2                 | 3       | 4       | 5      | 6      |
| He I 587.6 nm                                                  | 0.0972 | 0.0966            | 0.0937            | 0.0904  | 0.0900  | 0.0884 | 0.0870 |
| He II 468.6 nm                                                 | 0.3431 | 0.3470            | 0.3728            | 0.3986  | 0.4018  | 0.4146 | 0.4255 |
| C II] 232.6 nm                                                 | 0.2826 | 0.2827            | 0.2907            | 0.3084  | 0.3115  | 0.3202 | 0.3293 |
| C III] 190.9 nm                                                | 1.7704 | 1.7621            | 1.8008            | 2.0272  | 2.0755  | 2.1789 | 2.3238 |
| C IV 154.9 nm                                                  | 2.4635 | 2.3316            | 1.6057            | 2.1595  | 2.2977  | 2.3985 | 2.8400 |
| [N II] 658.4 nm                                                | 0.8455 | 0.8453            | 0.8732            | 0.9147  | 0.9213  | 0.9409 | 0.9619 |
| N III] 174.9 nm                                                | 0.0104 | 0.0104            | 0.0107            | 0.0123  | 0.0127  | 0.0135 | 0.0146 |
| [N III] 57.32 $\mu\text{m}$                                    | 0.1270 | 0.1268            | 0.1254            | 0.1256  | 0.1258  | 0.1257 | 0.1260 |
| N IV] 148.6 nm                                                 | 0.2264 | 0.2264            | 0.2483            | 0.3189  | 0.3349  | 0.3658 | 0.4246 |
| N V 124.0 nm                                                   | 0.1635 | 0.1566            | 0.1306            | 0.1792  | 0.1939  | 0.2118 | 0.2575 |
| [O I] 630.0 nm                                                 | 0.1133 | 0.1127            | 0.1183            | 0.1252  | 0.1260  | 0.1295 | 0.1330 |
| [O II] 372.7 nm                                                | 2.0807 | 2.0818            | 2.1505            | 2.2646  | 2.2845  | 2.3396 | 2.3940 |
| [O III] 436.3 nm                                               | 0.1599 | 0.1592            | 0.1608            | 0.1773  | 0.1808  | 0.1877 | 0.1975 |
| [O III] 500.7 nm                                               | 16.296 | 16.232            | 16.053            | 16.611  | 16.745  | 16.926 | 17.224 |
| [O III] 51.80 $\mu\text{m}$                                    | 1.2870 | 1.2823            | 1.2528            | 1.2359  | 1.2348  | 1.2244 | 1.2176 |
| [O III] 88.33 $\mu\text{m}$                                    | 0.2637 | 0.2628            | 0.2568            | 0.2542  | 0.2541  | 0.2523 | 0.2513 |
| O IV] 140.2 nm                                                 | 0.2093 | 0.2096            | 0.2342            | 0.3121  | 0.3305  | 0.3648 | 0.4331 |
| [O IV] 25.88 $\mu\text{m}$                                     | 3.6176 | 3.6370            | 3.8972            | 4.2203  | 4.2682  | 4.4150 | 4.5757 |
| O V] 121.8 nm                                                  | 0.1836 | 0.1863            | 0.2232            | 0.3232  | 0.3503  | 0.3943 | 0.4879 |
| O VI 103.2 nm                                                  | 0.0189 | 0.0185            | 0.0192            | 0.0278  | 0.0304  | 0.0344 | 0.0434 |
| [Ne II] 12.81 $\mu\text{m}$                                    | 0.0250 | 0.0249            | 0.0255            | 0.0260  | 0.0260  | 0.0264 | 0.0266 |
| [Ne III] 386.9 nm                                              | 2.0600 | 2.0536            | 2.0574            | 2.1590  | 2.1807  | 2.2197 | 2.2741 |
| [Ne III] 15.55 $\mu\text{m}$                                   | 1.8676 | 1.8475            | 1.8191            | 1.8027  | 1.8019  | 1.7923 | 1.7868 |
| [Ne IV] 242.3 nm                                               | 0.7983 | 0.8008            | 0.8748            | 1.0612  | 1.0989  | 1.1801 | 1.3167 |
| [Ne V] 342.6 nm                                                | 0.5785 | 0.5834            | 0.6429            | 0.7661  | 0.7919  | 0.8436 | 0.9286 |
| [Ne V] 14.32 $\mu\text{m}$                                     | 1.5680 | 1.5787            | 1.6792            | 1.7906  | 1.8040  | 1.8569 | 1.9041 |
| [Ne V] 24.31 $\mu\text{m}$                                     | 1.0480 | 1.0513            | 1.1239            | 1.2128  | 1.2251  | 1.2664 | 1.3088 |
| [Ne VI] 7.65 $\mu\text{m}$                                     | 0.1100 | 0.1112            | 0.1212            | 0.1341  | 0.1361  | 0.1423 | 0.1491 |
| Mg II 279.8 nm                                                 | 2.2299 | 2.1744            | 2.2295            | 2.3249  | 2.3440  | 2.3828 | 2.4212 |
| [Mg IV] 4.485 $\mu\text{m}$                                    | 0.1224 | 0.1236            | 0.1316            | 0.1407  | 0.1420  | 0.1459 | 0.1502 |
| [Mg V] 292.8 nm                                                | 0.0937 | 0.0941            | 0.1020            | 0.1202  | 0.1240  | 0.1313 | 0.1441 |
| [Mg V] 5.608 $\mu\text{m}$                                     | 0.1848 | 0.1857            | 0.1942            | 0.2052  | 0.2067  | 0.2112 | 0.2163 |
| Si II] 233.5 nm                                                | 0.1647 | 0.1640            | 0.1667            | 0.1776  | 0.1796  | 0.1848 | 0.1905 |
| [Si II] 34.81 $\mu\text{m}$                                    | 0.1566 | 0.1561            | 0.1611            | 0.1674  | 0.1681  | 0.1713 | 0.1743 |
| Si III] 189.2 nm                                               | 0.4584 | 0.4624            | 0.5051            | 0.5949  | 0.6132  | 0.6583 | 0.7194 |
| Si IV 139.7 nm                                                 | 0.2058 | 0.1960            | 0.1457            | 0.1825  | 0.1936  | 0.2047 | 0.2400 |
| [S II] 672.0 nm                                                | 0.3698 | 0.3698            | 0.3823            | 0.4011  | 0.4038  | 0.4129 | 0.4222 |
| [S III] 953.1 nm                                               | 1.1365 | 1.1356            | 1.1529            | 1.1918  | 1.1991  | 1.2162 | 1.2346 |
| [S III] 18.71 $\mu\text{m}$                                    | 0.5437 | 0.5435            | 0.5520            | 0.5628  | 0.5644  | 0.5694 | 0.5743 |
| [S III] 33.47 $\mu\text{m}$                                    | 0.2180 | 0.2178            | 0.2214            | 0.2269  | 0.2278  | 0.2303 | 0.2329 |
| [S IV] 10.51 $\mu\text{m}$                                     | 2.0387 | 2.0307            | 1.9690            | 1.9321  | 1.9296  | 1.9119 | 1.9012 |
| $\log[F(\text{H}\beta)/\text{erg s}^{-1}]$                     | 35.432 | 35.424            | 35.361            | 35.317  | 35.313  | 35.288 | 35.271 |
| $T_e/\text{K}$ inner edge                                      | 17 990 | 18 040            | 18 750            | 19 910  | 20 210  | 20 500 | 21 210 |
| $(T_e/\text{K})$                                               | 12 050 | 12 050            | 12 190            | 12 560  | 12 618  | 12 764 | 12 972 |
| $(\text{He}^+/\text{He})$                                      | 0.670  | 0.665             | 0.643             | 0.618   | 0.615   | 0.604  | 0.592  |
| $(\text{He}^{2+}/\text{He})$                                   | 0.297  | 0.300             | 0.320             | 0.343   | 0.346   | 0.356  | 0.368  |
| $R_{\text{out}}/10^{17} \text{ cm}$                            | 4.059  | 4.033             | 3.863             | 3.768   | 3.760   | 3.705  | 3.672  |
| $\tau_{121.6}$                                                 | 0.267  | 0.274             | 0.404             | 0.504   | 0.489   | 0.566  | 0.558  |
| $\langle a^2 \rangle / \langle a^3 \rangle (\mu\text{m}^{-1})$ | –      | 1.00              | 10.00             | 25.08   | 38.44   | 28.28  | 41.54  |
| GrGH/TotH                                                      | 0.000  | 0.0013            | 0.017             | 0.050   | 0.060   | 0.066  | 0.091  |
| GrGC/TotC                                                      | 0.000  | 0.0005            | 0.005             | 0.014   | 0.019   | 0.017  | 0.024  |

the relative fraction of non-ionizing photons that the grains absorb will increase. Hence the average energy per absorbed photon will decrease. For the gas the story is very different. In a first approximation the electron temperature will be constant inside the ionized region, and therefore the recombination rates will be constant as well. Since the gas is assumed to be in equilibrium, the photoionization rates must be constant as well and the total amount of heating is constant too (or even increases near the ionization front because

the lowest energy ionizing photons will be depleted). This implies that the relative importance of the photoelectric effect will decrease when one moves away from the illuminated face of the nebula.

We also noted that the enhancement effect is stronger for optical/UV lines, compared with infrared fine-structure lines. This is easy to understand. The excitation potential of the optical/UV lines is much higher and they are only excited by the high energy tail of the electrons. This makes these lines exponentially sensitive to

**Table 7.** Same as Table 5, but for the planetary nebula region models with graphite.

| model label                                                        | None   | 1.0 $\mu\text{m}$ | 0.1 $\mu\text{m}$ | MRN31  | WD31 A0 | KMH31  | WD31 A6 |
|--------------------------------------------------------------------|--------|-------------------|-------------------|--------|---------|--------|---------|
| model no.                                                          | 0      | 1                 | 2                 | 3      | 4       | 5      | 6       |
| He I 587.6 nm                                                      | 0.0972 | 0.0967            | 0.0942            | 0.0888 | 0.0880  | 0.0865 | 0.0844  |
| He II 468.6 nm                                                     | 0.3431 | 0.3459            | 0.3665            | 0.4089 | 0.4147  | 0.4272 | 0.4463  |
| C II] 232.6 nm                                                     | 0.2826 | 0.2827            | 0.2915            | 0.3240 | 0.3294  | 0.3407 | 0.3427  |
| C III] 190.9 nm                                                    | 1.7704 | 1.7663            | 1.8675            | 2.3375 | 2.4196  | 2.5850 | 2.6638  |
| C IV 154.9 nm                                                      | 2.4635 | 2.3414            | 1.8614            | 2.5680 | 2.8158  | 2.8801 | 3.3301  |
| [N II] 658.4 nm                                                    | 0.8455 | 0.8449            | 0.8709            | 0.9397 | 0.9515  | 0.9721 | 0.9906  |
| N III] 174.9 nm                                                    | 0.0104 | 0.0104            | 0.0112            | 0.0147 | 0.0153  | 0.0165 | 0.0172  |
| [N III] 57.32 $\mu\text{m}$                                        | 0.1270 | 0.1269            | 0.1265            | 0.1273 | 0.1274  | 0.1276 | 0.1265  |
| N IV] 148.6 nm                                                     | 0.2264 | 0.2292            | 0.2798            | 0.4079 | 0.4315  | 0.4755 | 0.5216  |
| N V 124.0 nm                                                       | 0.1635 | 0.1600            | 0.1585            | 0.2469 | 0.2685  | 0.2922 | 0.3582  |
| [O I] 630.0 nm                                                     | 0.1133 | 0.1127            | 0.1175            | 0.1286 | 0.1303  | 0.1337 | 0.1364  |
| [O II] 372.7 nm                                                    | 2.0807 | 2.0807            | 2.1479            | 2.3458 | 2.3791  | 2.4430 | 2.4695  |
| [O III] 436.3 nm                                                   | 0.1599 | 0.1595            | 0.1662            | 0.2014 | 0.2072  | 0.2183 | 0.2226  |
| [O III] 500.7 nm                                                   | 16.296 | 16.252            | 16.354            | 17.608 | 17.806  | 18.134 | 18.087  |
| [O III] 51.80 $\mu\text{m}$                                        | 1.2870 | 1.2832            | 1.2639            | 1.2415 | 1.2387  | 1.2307 | 1.2106  |
| [O III] 88.33 $\mu\text{m}$                                        | 0.2637 | 0.2631            | 0.2593            | 0.2564 | 0.2561  | 0.2550 | 0.2510  |
| O IV] 140.2 nm                                                     | 0.2093 | 0.2129            | 0.2710            | 0.4095 | 0.4357  | 0.4846 | 0.5397  |
| [O IV] 25.88 $\mu\text{m}$                                         | 3.6176 | 3.6385            | 3.8995            | 4.4292 | 4.5055  | 4.6592 | 4.8556  |
| O V] 121.8 nm                                                      | 0.1836 | 0.1897            | 0.2696            | 0.4316 | 0.4633  | 0.5226 | 0.6255  |
| O VI 103.2 nm                                                      | 0.0189 | 0.0192            | 0.0251            | 0.0373 | 0.0398  | 0.0454 | 0.0556  |
| [Ne II] 12.81 $\mu\text{m}$                                        | 0.0250 | 0.0250            | 0.0255            | 0.0261 | 0.0261  | 0.0264 | 0.0265  |
| [Ne III] 386.9 nm                                                  | 2.0600 | 2.0556            | 2.0899            | 2.2993 | 2.3338  | 2.3926 | 2.4068  |
| [Ne III] 15.55 $\mu\text{m}$                                       | 1.8676 | 1.8571            | 1.8392            | 1.8149 | 1.8123  | 1.8046 | 1.7876  |
| Ne IV] 242.3 nm                                                    | 0.7983 | 0.8069            | 0.9438            | 1.2677 | 1.3235  | 1.4304 | 1.5390  |
| [Ne V] 342.6 nm                                                    | 0.5785 | 0.5869            | 0.6896            | 0.8825 | 0.9130  | 0.9738 | 1.0497  |
| [Ne V] 14.32 $\mu\text{m}$                                         | 1.5680 | 1.5764            | 1.6765            | 1.8595 | 1.8800  | 1.9344 | 1.9913  |
| [Ne V] 24.31 $\mu\text{m}$                                         | 1.0480 | 1.0524            | 1.1328            | 1.2769 | 1.2943  | 1.3377 | 1.3833  |
| [Ne VI] 7.65 $\mu\text{m}$                                         | 0.1100 | 0.1111            | 0.1230            | 0.1424 | 0.1447  | 0.1510 | 0.1581  |
| Mg II 279.8 nm                                                     | 2.2299 | 2.2030            | 1.9523            | 1.9529 | 2.0220  | 1.9956 | 2.0640  |
| [Mg IV] 4.485 $\mu\text{m}$                                        | 0.1224 | 0.1234            | 0.1311            | 0.1459 | 0.1479  | 0.1521 | 0.1572  |
| [Mg V] 292.8 nm                                                    | 0.0937 | 0.0948            | 0.1102            | 0.1388 | 0.1432  | 0.1519 | 0.1616  |
| [Mg V] 5.608 $\mu\text{m}$                                         | 0.1848 | 0.1856            | 0.1965            | 0.2135 | 0.2153  | 0.2200 | 0.2238  |
| Si II] 233.5 nm                                                    | 0.1647 | 0.1640            | 0.1674            | 0.1884 | 0.1922  | 0.1987 | 0.2034  |
| [Si II] 34.81 $\mu\text{m}$                                        | 0.1566 | 0.1561            | 0.1604            | 0.1707 | 0.1723  | 0.1749 | 0.1809  |
| Si III] 189.2 nm                                                   | 0.4584 | 0.4627            | 0.5224            | 0.7002 | 0.7289  | 0.7982 | 0.8331  |
| Si IV 139.7 nm                                                     | 0.2058 | 0.1980            | 0.1694            | 0.2631 | 0.2893  | 0.3080 | 0.3584  |
| [S II] 672.0 nm                                                    | 0.3698 | 0.3697            | 0.3808            | 0.4119 | 0.4170  | 0.4262 | 0.4348  |
| [S III] 953.1 nm                                                   | 1.1365 | 1.1356            | 1.1562            | 1.2272 | 1.2389  | 1.2599 | 1.2712  |
| [S III] 18.71 $\mu\text{m}$                                        | 0.5437 | 0.5435            | 0.5522            | 0.5700 | 0.5725  | 0.5773 | 0.5814  |
| [S III] 33.47 $\mu\text{m}$                                        | 0.2180 | 0.2178            | 0.2216            | 0.2310 | 0.2325  | 0.2351 | 0.2373  |
| [S IV] 10.51 $\mu\text{m}$                                         | 2.0387 | 2.0334            | 1.9881            | 1.9380 | 1.9325  | 1.9210 | 1.8964  |
| $\log[F(\text{H}\beta)]/\text{erg s}^{-1}$                         | 35.432 | 35.425            | 35.378            | 35.318 | 35.313  | 35.294 | 35.275  |
| $T_e/K$ inner edge                                                 | 17 990 | 18 110            | 19 320            | 20 500 | 20 710  | 21 000 | 21 920  |
| $\langle T_e/K \rangle$                                            | 12 050 | 12 078            | 12 303            | 12 912 | 13 002  | 13 183 | 13 335  |
| $\langle \text{He}^+/\text{He} \rangle$                            | 0.670  | 0.665             | 0.644             | 0.605  | 0.598   | 0.587  | 0.569   |
| $\langle \text{He}^{2+}/\text{He} \rangle$                         | 0.297  | 0.299             | 0.319             | 0.355  | 0.360   | 0.371  | 0.384   |
| $R_{\text{out}}/10^{17}$ cm                                        | 4.059  | 4.039             | 3.919             | 3.799  | 3.793   | 3.753  | 3.718   |
| $\tau_{121.6}$                                                     | 0.267  | 0.273             | 0.388             | 0.502  | 0.469   | 0.512  | 0.437   |
| $\langle a^2 \rangle / \langle a^3 \rangle$ ( $\mu\text{m}^{-1}$ ) | –      | 1.00              | 10.00             | 28.28  | 61.10   | 43.31  | 326.53  |
| GrGH/TotH                                                          | 0.000  | 0.003             | 0.038             | 0.090  | 0.103   | 0.114  | 0.163   |
| GrGC/TotC                                                          | 0.000  | 0.0005            | 0.006             | 0.017  | 0.028   | 0.025  | 0.086   |

electron temperature, and therefore also very sensitive to the enhanced photoelectric heating. The infrared fine-structure lines on the other hand have low excitation potentials and are nearly insensitive to electron temperature and photoelectric heating. Most of the effect on these lines will be due to changes in the overall ionization structure. A mild temperature dependence of the collisional cross-section caused by resonances may also contribute (e.g. [Ne V] 14.32  $\mu\text{m}$ , see van Hoof et al. 2000a and references therein).

From a comparison of the models it is also apparent that the helium recombination lines are affected by the photoelectric effect. This has already been explained earlier. The increased photoelectric effect leads to an increase in electron temperature, which in turn leads to a decrease in the recombination rates and an increase in the overall degree of ionization. This is confirmed by comparing the volume averages of the helium ion fractions. It is clear that in the H II-region models  $\text{He}^+$  is gaining at the expense of  $\text{He}^0$ , while

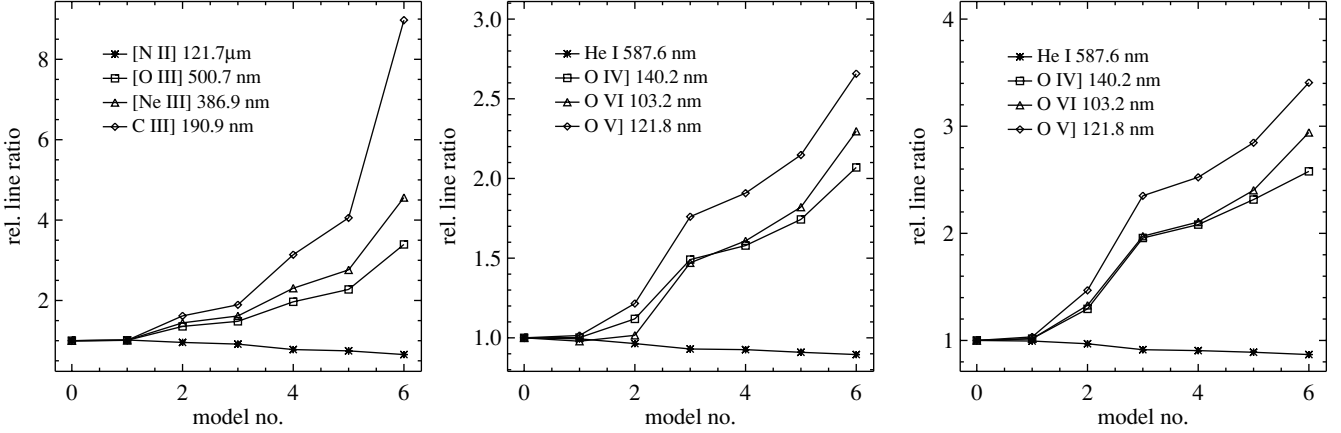


**Figure 3.** The variation of the line ratio to  $H\beta$  for selected emission lines as a function of the grain size distribution. The left-hand panel shows the results for the H II-region models, the middle panel for the PN models with silicate, and the right-hand panel for the PN models with graphite. All line flux ratios are normalized to the base model without dust. The models numbers are defined in Table 4.

in the PN models  $\text{He}^{2+}$  is gaining at the expense of  $\text{He}^+$  when the photoelectric effect increases.

In general, the relative line strength increases or decreases monotonically with an increase in the photoelectric effect. However, there are a couple of notable exceptions to this rule in the PN models. In the following discussion we will concentrate on the silicate models. The details are somewhat different for the graphite models, but the underlying physics is the same. The exceptional behaviour occurs for the following lines (in order of decreasing magnitude of the effect): C IV 154.9, Si IV 139.7 and N V 124.0 nm. For all these lines the relative strength decreases going from the dust-free model to the 1.0- and the 0.1- $\mu\text{m}$  models, while showing an overall increasing trend for the subsequent models. What is immediately apparent is that this effect only occurs in allowed (resonance) transitions. However, the effect is much less in the other two resonance lines in the list, namely Mg II 279.8 and O VI 103.2 nm (these lines only show a mild decrease going from the dust-free to the 1.0- $\mu\text{m}$  model). All five lines are the equivalent of  $\text{Ly}\alpha$ . They have large line-centre optical depths, and as a consequence they are scattered many times in the nebula before escaping. This random walk greatly increases the chance of the photon being absorbed by background opacities, most notably from dust grains. The higher the line-centre optical depth is, the longer the random walk will be and the higher the probability of destruction is. The fact that the strongest decrease occurs going from the 1.0- to the 0.1- $\mu\text{m}$  model can be understood by looking at Fig. 1. The dust opacity rises dramatically in the UV going from 1.0- to 0.1- $\mu\text{m}$  sized grains, while the photoelectric effect is still modest for these grains. Hence the increase in photon destruction wins. For subsequent models the rise in optical depth is less dramatic (or there is even a decrease), while the photoelectric effect starts to dominate the models. In these models the rising photoelectric effect wins. This trend is confirmed by inspecting  $\tau_{121.6}$  in Tables 5–7.<sup>3</sup> In Table 8 we show the line-centre optical depths of the lines in question. All optical depths follow the trend of the decreasing magnitude of the effect indicated above, with the exception of Mg II 279.8 nm. For this line the decreasing effect is much weaker than expected based on the line-

**Table 8.** Line-centre optical depths for the resonance lines in the PN model with 0.1- $\mu\text{m}$  silicate grains. All the resonance lines are doublets, which are shown separately here.

| Line           | Opt. depth |
|----------------|------------|
| C IV 154.8 nm  | 6760       |
| C IV 155.1 nm  | 3390       |
| Si IV 139.4 nm | 2510       |
| Si IV 140.3 nm | 1260       |
| N V 123.9 nm   | 1030       |
| N V 124.3 nm   | 512        |
| Mg II 279.6 nm | 2790       |
| Mg II 280.4 nm | 1400       |
| O VI 103.2 nm  | 517        |
| O VI 103.8 nm  | 258        |

centre optical depth. This line has a much longer-wavelength than any of the other lines. At 279.8 nm silicate grains are more or less transparent and the chance of absorption on grains is greatly reduced due to this fact. This is not the case for graphite grains, and one can see that the decreasing effect is stronger in the graphite models for this line.

From the discussion presented above, one might be tempted to say that the photoelectric effect will be stronger if more small grains are present, due to the increased opacity and the higher photoelectric yield. In a rough sense this is true, but the reader should be warned that no simple predictors can be constructed from such an observation that allow an accurate estimate of the effect. Examples of such predictors could be the average surface to volume ratio  $\langle a^2 \rangle / \langle a^3 \rangle$  of the grains and the continuum optical depth  $\tau_{121.6}$ . It can be seen from Tables 5–7 that in general neither of these predict the correct sequence in the tables. Detailed models will always be necessary to obtain a reliable prediction of the magnitude of the photoelectric effect.

All these results clearly illustrate that the size distribution alone has a dramatic effect on the emitted spectrum, and is therefore an important parameter in the modelling of spectra from H II regions and PNe. However, very little is known concerning the size distribution of grains in these objects. As was already mentioned above,

<sup>3</sup> Note that  $\tau_{121.6}$  is the total continuum optical depth due to all physical processes, corrected for stimulated emission. This implies that the optical depth should be non-zero for the dust-free models.

the most detailed studies of grain size distributions in the literature focus on explaining the extinction curve caused by grains in the diffuse ISM. It is not clear whether these distributions are valid for H II regions since grains undergo an appreciable amount of processing when they move in and out of molecular clouds. It is even more questionable whether ISM size distributions would be valid for PN. After all, the grains in the ISM come from a variety of sources (including PN, but also supernovae and other sources), and also the grains in the ISM have undergone far more prolonged processing than the grains in the PN. Therefore, the further study of grain size distributions in photoionized regions and AGB/post-AGB stars is urgently needed.

## 5 CONCLUSIONS

In this paper we investigated the effect the grain size distribution has on the amount of photoelectric heating in photoionized regions, and its consequences for the spectrum emitted by the plasma. To model these effects we used the comprehensively upgraded grain code in CLOUDY 96. One of these upgrades is the newly developed hybrid grain charge model. This model allows discrete charge states of very small grains to be modelled accurately while simultaneously avoiding the overhead of fully resolving the charge distribution of large grains, thus making the model both accurate and computationally efficient.

A comprehensive comparison with the fully resolved charge state models of WD validates the new model. The WD and CLOUDY results for the photoelectric heating rates are generally in excellent agreement, with only a few outliers for single sized grains in the  $n = 2$  and 3 cases. The results for the size distribution cases always agree to better than 25 per cent, even for  $n = 2$ . This is well within the accuracy with which we know grain physics to date. The collisional cooling rates usually are in even better agreement. Furthermore, it is clear that the accuracy of the  $n$ -charge state approximation increases as the number of charge states increases, as should be expected. The agreement between the CLOUDY and the WD results is very satisfactory for realistic size distributions, and should be sufficient for all realistic astrophysical applications, even with  $n = 2$ .

The effect of the grain size distribution on the line emission from photoionized regions is studied by taking standard models for an H II region and a planetary nebula and adding a dust component to the models with varying grain size distributions (either single sized grains or size distributions taken from the literature). A comparison of the models shows that varying the size distribution (while keeping the chemical composition and the dust-to-gas mass ratio of the grains constant) has a dramatic effect on the emitted spectrum. The strongest enhancement is always found in optical/UV lines of the highest ionization stages present in the spectrum (with factors up to 2.5–4), while the strongest decrease is typically found in optical/UV lines of low ionization lines or infrared fine-structure lines of low/intermediate ionization stages (with reductions up to 10–25 per cent). The enhancement effect is strongest in the inner regions of the nebula, and it correlates well with the total amount of photoelectric heating contributed to the plasma by the grains. Changing the grain size distribution also affects the ionization balance because the increase in electron temperature leads to enhanced recombination and also because the grains are directly competing with the gas for ionizing photons. Finally, changing the grain size distribution can also affect resonance lines such as C IV 154.9 nm which are very sensitive to changes in the background opacity.

All these results clearly demonstrate that the grain size distribution is an important parameter in photoionization models. Only few studies of grain size distributions exist, and they mainly concentrate on the diffuse interstellar medium in order to explain extinction curves. Further study of grain size distributions will be needed in order to enable more accurate modelling of photoionized regions. This is especially the case for planetary nebulae since it is not clear whether ISM size distributions are valid for these objects.

## ACKNOWLEDGMENTS

We wish to acknowledge financial support by the National Science Foundation through grant no. AST-0071180, and NASA through its LTSA program, NAG 5-3223. This research was also supported in part by the Natural Sciences and Engineering Research Council of Canada. P.v.H. is currently supported by the Engineering and Physical Sciences Research Council of the United Kingdom. J.C.W. acknowledges support from an NSF International Research Fellowship. This paper used the photoionization code CLOUDY which can be obtained from <http://www.nublado.org> and the Atomic Line List available at <http://www.pa.uky.edu/~peter/atomic>.

## REFERENCES

- Bakes E.L.O., Tielens A.G.G.M., 1994, *ApJ*, 427, 822  
 Baldwin J.A., Ferland G.J., Martin P.G., Corbin M.R., Cota S.A., Peterson B.M., Slettebak A., 1991, *ApJ*, 374, 580 (BFM)  
 Bohren C.F., Huffman D.R., 1983, *Absorption and Scattering of Light by Small Particles*. Wiley, New York  
 Borkowski K.J., Harrington J.P., 1991, *ApJ*, 379, 168  
 Bruggeman D.A.G., 1935, *Ann. Phys.*, 24, 636  
 Dopita M.A., Sutherland R.S., 2000, *ApJ*, 539, 742  
 Draine B.T., Lee H.M., 1984, *ApJ*, 285, 89  
 Draine B.T., Sutin B., 1987, *ApJ*, 320, 803  
 Ercolano B., Barlow M.J., Storey P.J., Liu X.-W., Rauch T., Werner K., 2003, *MNRAS*, 344, 1145  
 Farafonov V.G., 2000, *Opt. Spectrosc.*, 88, 441  
 Ferland G.J., 2000a, in Manset N., Veillet C., Crabtree D., eds, *ASP Conf. Ser. Vol. 216, Astronomical Data Analysis Software and Systems IX*. Astron. Soc. Pac., San Francisco, p. 32  
 Ferland G.J., 2000b, *Rev. Mex. Astr. Astrofis. Ser. Conf.*, 9, 153  
 Hansen J.E., Travis L.D., 1974, *Space Sci. Rev.*, 16, 527  
 Kim S.-H., Martin P.G., Hendry P.D., 1994, *ApJ*, 422, 164  
 Li A., Draine B.T., 2001, *ApJ*, 554, 778  
 Maciel W.J., Pottasch S.R., 1982, *A&A*, 86, 380  
 Martin P.G., Rouleau F., 1991, in Malina R.F., Bowyer S., eds, *Extreme Ultraviolet Astronomy*. Pergamon, New York, p. 341  
 Mathis J.S., Rimpl W., Nordsieck K.H., 1977, *ApJ*, 217, 425  
 Mie G., 1908, *Ann. Phys.*, 25, 377  
 Molster F.J. et al., 2001, *A&A*, 372, 165  
 Péquignot D. et al., 2001, in Ferland G.J., Savin D.W., eds, *ASP Conf. Ser. Vol. 247, Spectroscopic Challenges of Photoionized Plasmas*. Astron. Soc. Pac., San Francisco, p. 533  
 Spitzer L., 1948, *ApJ*, 107, 6  
 Stognienko R., Henning Th., Ossenkopf V., 1995, *A&A*, 296, 797  
 Tielens A.G.G.M., Hollenbach D.J., 1985, *ApJ*, 291, 722  
 van de Hulst H.C., 1957, *Light Scattering by Small Particles*. Wiley, New York  
 van Hoof P.A.M., Beintema D.A., Verner D.A., Ferland G.J., 2000a, *A&A*, 354, L41  
 van Hoof P.A.M., Martin P.G., Ferland G.J., 2000b, in Franco J., Terlevich E., López-Cruz O., Aretxaga I., eds, *ASP Conf. Ser. Vol. 215, Cosmic Evolution and Galaxy Formation: Structure, Interactions, and Feedback*. Astron. Soc. Pac., San Francisco, p. 220 (extended version astro-ph/0001196)



van Hoof P.A.M., Weingartner J.C., Martin P.G., Volk K., Ferland G.J., 2001, in Ferland G.J., Savin D.W., eds, ASP Conf. Ser. Vol. 247, Spectroscopic Challenges of Photoionized Plasmas. Astron. Soc. Pac., San Francisco, p. 363  
Volk K., 2001, in Ferland G.J., Savin D.W., eds, ASP Conf. Ser. Vol. 247, Spectroscopic Challenges of Photoionized Plasmas. Astron. Soc. Pac., San Francisco, p. 379

Voshchinnikov N.V., Mathis J.S., 1999, ApJ, 526, 257  
Waters L.B.F.M. et al., 1996, A&A, 315, L361  
Weingartner J.C., Draine B.T., 2001a, ApJS, 134, 263 (WD)  
Weingartner J.C., Draine B.T., 2001b, ApJ, 548, 296

This paper has been typeset from a  $\text{\TeX}/\text{\LaTeX}$  file prepared by the author.